

Very high-energy gamma-ray and neutrino emission from hadronic interaction in compact binary millisecond pulsars

V. VECCHIOTTI¹ AND M. LINARES^{1,2}

¹*NTNU, Department of Physics, NO-7491 Trondheim, Norway*

²*Departament de Física, EEBE, Universitat Politècnica de Catalunya, Av. Eduard Maristany 16, E-08019 Barcelona, Spain.*

Abstract

Blackwidow and redback systems are millisecond pulsars in compact orbits with ultra-light and low-mass companions, respectively, collectively known as “spider pulsars”. In such systems, an intrabinary shock can form between the pulsar and the companion winds, serving as a site for particle acceleration and associated non-thermal emission. Assuming that protons can be extracted from the neutron star surface and accelerated at the intrabinary shock and/or within the pulsar wind, we model the very high-energy gamma-ray and neutrino emissions ($0.1 - 10^3$ TeV) produced through interactions with the companion wind and the companion star. We first calculate the high-energy emissions using an optimistic combination of parameters to maximize the gamma-ray and neutrino fluxes. We find that, for energetic spider pulsars with a spin-down power $\gtrsim 10^{35} \text{ erg s}^{-1}$ and a magnetic field of $\sim 10^3$ G in the companion region, the gamma-ray emission could be detectable as point sources by CTA and LHAASO, while the neutrino emission could be detectable by the future TRIDENT detector. Finally, we build a synthetic population of these systems, compute the cumulative neutrino flux expected from spider pulsars, and compare it with the Galactic neutrino diffuse emission measured by IceCube. We find that, under realistic assumptions on the fraction of the spin-down power converted into protons, the contribution of spiders to the diffuse Galactic neutrino flux is negligible.

Keywords: High-energy astrophysics - millisecond pulsars - gamma rays

1. INTRODUCTION

In recent years, an increasing number of millisecond pulsars (MSPs) have been detected in the GeV energy range by Fermi-LAT (D. A. Smith et al. 2023). Among these systems, a significant subset consists of MSPs in compact binary systems with orbital periods $P_b \lesssim 1$ day, where the companion stars are not fully degenerate (I. F. Nedreaas 2024). Due to their small orbital separations, typically just a few Solar radii, the pulsar’s relativistic wind can strongly irradiate and ablate the companion star. These systems, known as spiders, are classified into two categories based on the companion star’s mass: redbacks (RBs) and blackwidows (BW). RB companions typically have masses $M_c \gtrsim 0.1 M_\odot$, while BW companions are even lighter, with $M_c < 0.1 M_\odot$.

Many spiders exhibit a non-thermal, orbitally modulated emission component in the X-ray band that peaks at either inferior or superior conjunction (R. H. H.

Huang et al. 2012; S. Bogdanov et al. 2005, 2011, 2021; Z. Wadiasingh et al. 2017; Z. Wadiasingh et al. 2018). The X-ray emission is often associated with the presence of an intrabinary pulsar wind termination shock (IBS), where the ram pressure of the pulsar wind is counterbalanced by that of the companion’s wind or magnetosphere (A. K. Harding & T. K. Gaisser 1990). The IBS is considered an efficient site for particle acceleration (A. K. Harding & T. K. Gaisser 1990; J. Arons & M. Tavani 1993; J. Cortés & L. Sironi 2022, 2024, 2025). While the exact acceleration mechanism remains uncertain, it may involve either diffusive shock acceleration (e.g., A. K. Harding & T. K. Gaisser 1990; C. J. T. van der Merwe et al. 2020) or magnetic reconnection (e.g., C. J. T. van der Merwe et al. 2020; J. Cortés & L. Sironi 2022, 2024, 2025). In either case, the observed X-ray flux is thought to result from synchrotron emission produced by relativistic electron-positron pairs accelerated at the IBS and Doppler boosted along the shock tangent (e.g., Z. Wadiasingh et al. 2017; Z. Wadiasingh et al. 2018; R. W. Romani & N. Sanchez 2016; N. Sanchez & R. W. Romani 2017a; C. J. T. van der Merwe et al. 2020; D.

Kandel et al. 2019; D. Kandel et al. 2021). Additionally, these electron-positron pairs responsible for X-ray emission may also interact via inverse Compton scattering with the radiation field of the companion star, producing orbitally modulated TeV gamma-rays that are potentially detectable by current and future gamma-ray facilities (C. J. T. van der Merwe et al. 2020). However, no spider systems have been detected in the TeV gamma-ray band to date.

Instead, in the GeV energy range, gamma-ray emission from pulsar binaries is predominantly driven by pulsed magnetospheric radiation originating from the pulsar itself and is generally expected to be orbitally constant (apart from the pronounced dips observed in the light curves of eclipsing systems; R. H. D. Corbet et al. 2022; C. J. Clark et al. 2023). Moreover, in some RB systems orbitally modulated GeV signals have been detected with the Fermi-LAT in a few systems (e.g., C. W. Ng et al. 2018; H. An et al. 2018; C. J. Clark et al. 2021), suggesting a potential IBS origin. However, in some RB systems, the GeV gamma-ray emission appears to be anti-correlated with the X-ray emission. This anti-correlation suggests that alternative or additional mechanisms might contribute to the observed GeV modulation. In order to explain the GeV signal, various scenarios have been proposed (H. An et al. 2020; M. Sim et al. 2024). For instance, the orbitally modulated GeV gamma rays could originate from synchrotron emission produced by highly energetic leptons that, after being accelerated at the IBS, may penetrate the companion star’s region and interact with its magnetic field, producing the observed signal (M. Sim et al. 2024).

In this work, we explore the possibility that, in addition to electron-positron pairs, protons are also extracted from the neutron star’s surface. The possibility of baryons extracted from the neutron star surface was invoked in M. Hoshino et al. (1992) and Y. A. Gallant & J. Arons (1994), in order to explain particle acceleration at the pulsar wind termination shock and was further explored in later studies (e.g., M. Lemoine et al. 2015; K. Kotera et al. 2015; A. A. Philippov & A. Spitkovsky 2018; C. Guépin et al. 2020). The gamma-ray and neutrino emission produced as a result of the interaction of these accelerated hadrons with a target material has been investigated in various studies, e.g., in the case of the Crab Nebula (see E. Amato et al. 2003).

In spider systems, hadrons can be accelerated either at the IBS (A. K. Harding & T. K. Gaisser 1990) or, as in the pulsar case, within the pulsar magnetosphere and then get advected with the pulsar wind (PW) (K. Kotera et al. 2015). Here, we consider both acceleration scenarios and examine the possibility that these hadrons pene-

trate the companion region, where they interact with the companion’s wind (CW) and the companion star (CS). Such interactions produce gamma rays and neutrinos.

We investigate whether spiders can generate gamma rays and neutrinos at levels detectable by current and future gamma-ray and neutrino observatories. Furthermore, we assess whether the cumulative neutrino flux from a synthetic Galactic spider population could contribute significantly to the Galactic neutrino flux measured by IceCube (R. Abbasi et al. 2023).

The paper is organized as follows. In Sec. 2 and Sec. 3, we introduce the different acceleration scenarios and the interaction sites. In Sec. 4, we outline the transport equation. In Sec. 5, we describe the methodology for calculating gamma-ray and neutrino production. In Sec. 6, we detail the generation of a synthetic population of spiders. In Sec. 7, we present and discuss our results. Finally, we summarize our conclusions in Sec. 8.

2. PROTON ACCELERATION SCENARIOS

In this section, we model the high-energy gamma rays and neutrinos being produced by protons extracted from the neutron star surface. We consider two scenarios:

- 1) Scenario 1: PW. The protons are all accelerated in the pulsar magnetosphere (e.g., C. Guépin et al. 2020) and then advected with the PW. Consequently, the injected spectrum is a delta function with energy equal to the Lorentz factor of the wind (e.g., K. Kotera et al. 2015).
- 2) Scenario 2: IBS. The protons are accelerated at the IBS via magnetic reconnection (J. Cortés & L. Sironi 2022, 2024, 2025; C. J. T. van der Merwe et al. 2020). In this case, the injected spectrum is a power law with an exponential cut-off, where the spectral index α lies within the range 1.5 to 2.5, and the wind magnetization defines the cut-off energy.

In both cases, we assume that all protons can penetrate the companion region due to their high energy and consequently large Larmor radius. Once inside the companion region (the downstream region of the shock), protons are expected to diffuse due to the turbulent magnetic field. In this environment, they can interact either with the CW or with the CS, leading to the production of gamma rays and neutrinos.

In the following, we briefly describe the two acceleration scenarios considered in this work and the target material.

2.1. Scenario 1: protons from the PW

The mechanism that accelerates particles in the wind to the terminal Lorentz factor remains a matter of de-

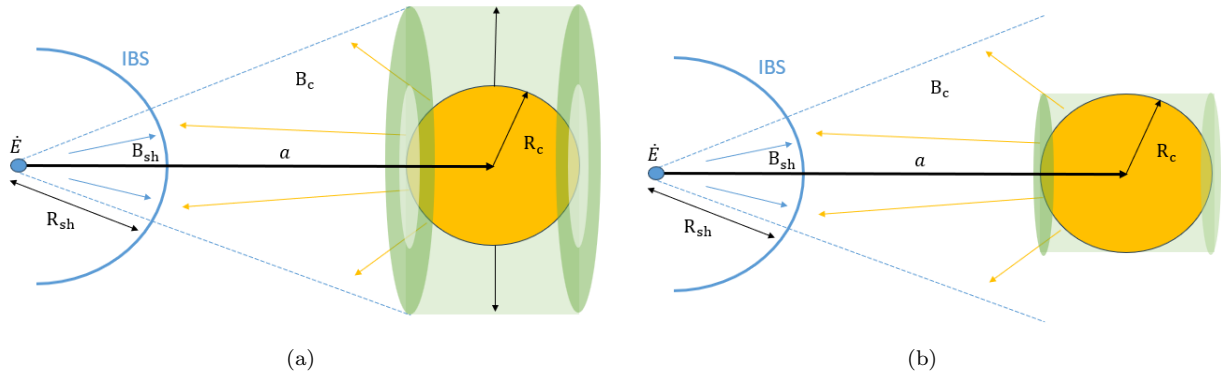


Figure 1. Sketch of a spider system. The millisecond pulsar is represented as a blue sphere on the left (not to scale), while the companion star is shown as a yellow sphere on the right. The pulsar (companion) wind is indicated with blue (yellow) arrows. The interaction between the winds forms the IBS, depicted as a blue semicircle. Panel (a): The green hollow cylinder around the companion represents the interaction region of protons with the CW. Panel (b): The green cylinder around the companion represents the interaction region of protons with the CS.

bate. In this work, we assume that the wind energy is primarily dominated by particle kinetic energy, rather than by Poynting flux (see, e.g., K. Kotera et al. 2015). This is equivalent to assuming that a large fraction, $\eta \sim 1$, of the pulsar spin-down energy is converted into particle energy.

In standard scenarios, particles are typically accelerated within the pulsar magnetosphere, either close to the neutron star surface and/or near the light cylinder, or in the current sheet (see e.g., A. Philippov et al. 2020). However, inside the light cylinder, in the presence of a background photon field, ions may experience significant curvature losses (K. Kotera et al. 2015). Following K. Kotera et al. (2015), we assume that, regardless of the maximum energy achieved in the pulsar magnetosphere, once the particles reach the wind region, they are advected with it at the wind’s Lorentz factor Γ_w that we will calculate later on in the text (see Sec. 4). As a result, in this scenario, all protons will be injected with energy equal to the Lorentz factor of the wind.

2.2. Scenario 2: protons accelerated at the IBS

The second scenario that we consider in this work is that hadrons are accelerated at the IBS. In general, collisionless shocks are considered efficient sites for diffusive shock acceleration, producing particles with a power-law spectrum and an exponential cutoff. The spectral index α is typically larger than 2, while the cut-off energy depends on shock properties such as radius, magnetic field, and compression ratio. However, the IBS is a relativistic shock that is expected to be strongly magnetized and quasi-perpendicular, making diffusive shock acceleration particularly challenging and inefficient (see e.g., L. Sironi et al. (2015) for a review). Indeed, the non-thermal X-ray spectrum of most spider systems exhibits

a relatively flat photon index $\Gamma_x = 1-2$ (e.g., M. Linares 2014; P. A. Gentile et al. 2014). This observation suggests a harder electron energy spectrum ($\alpha < 2$), which is difficult to explain within the framework of diffusive shock acceleration. The most likely acceleration mechanism taking place at the IBS is magnetic reconnection (J. Cortés & L. Sironi 2022, 2024, 2025). The pulsar wind consists of toroidal stripes of alternating magnetic field polarity, separated by current sheets of hot plasma (S. V. Bogovalov 1999; J. Petri & Y. Lyubarsky 2008). When oppositely directed fields are compressed at the shock, they can undergo annihilation through shock-driven reconnection (J. Cortés & L. Sironi 2022, 2024, 2025). For example, J. Cortés & L. Sironi (2024) have shown that if the pulsar spin axis is nearly aligned with the orbital angular momentum, the magnetic energy of the relativistic pulsar wind is efficiently converted into particle energy at the IBS.

In this paper, to reflect these uncertainties on the acceleration mechanism, we explore two possible values for the proton spectral index: $\alpha = 1.5$ and $\alpha = 2.5$. We calculate the cut-off energy assuming that protons are accelerated by magnetic reconnection (see Sec. 4 & Eq. 14). However, we note that a small fraction of particles may undergo further acceleration to higher energies through Fermi-like processes (J. Cortés & L. Sironi 2024).

3. INTERACTION SITES

In order to estimate the hadronic gamma-ray and neutrino fluxes from spiders, we model two interaction sites that the accelerated protons (Sec. 2) will reach: the CW and the CS. First, we collect, estimate, and list the main parameters of spider systems that are relevant to our calculation. In particular, in the case of

Table 1. We report the typical parameters for RB (second column) and BW (third column) systems. In order, we display the companion mass M_c , the orbital period P_b , the companion radius R_c , the orbital separation a , the shock radius R_{sh} , the wind number density n_w for $\dot{E} = 10^{33} - 10^{35} \text{ erg s}^{-1}$, and the companion number density n_c .

	RB	BW
M_c	$0.1 M_\odot$	$0.01 M_\odot$
P_b	8.2 h	4.9 h
R_c	$3.1 \times 10^{10} \text{ cm}$	$1.0 \times 10^{10} \text{ cm}$
a	$1.7 \times 10^{11} \text{ cm}$	$1.2 \times 10^{11} \text{ cm}$
R_{sh}	$7.7 \times 10^{10} \text{ cm}$	$6.6 \times 10^{10} \text{ cm}$
n_w	$3.1 \times 10^{9-11} \text{ cm}^{-3}$	$4.0 \times 10^{10-12} \text{ cm}^{-3}$
n_c	$9.8 \times 10^{23} \text{ cm}^{-3}$	$2.5 \times 10^{24} \text{ cm}^{-3}$

RBs (BW), the companion mass M_c is approximately $0.1 M_\odot$ ($0.01 M_\odot$). As for the neutron star mass, we assume $1.7 M_\odot$ (J. Strader et al. 2019). In this work, we adopt for the orbital periods of RBs and BWs the average values obtained from a sample of known sources, as listed in Tables 2 and 3 (I. F. Nedreaas 2024). We obtain orbital periods of 8.2 h for RBs and 4.9 h for BWs. Additionally, we assume that the CS is filling its Roche Lobe. With the above information, we can calculate the radius of the CS being $R_c \sim 3.1 \times 10^{10} \text{ cm}$ for RBs and $R_c \sim 1.0 \times 10^{10} \text{ cm}$ for BWs. Using the above values, we calculate the average number density of the CS, $n_c \sim 9.8 \times 10^{23} \text{ cm}^{-3}$ and $n_c \sim 2.5 \times 10^{24} \text{ cm}^{-3}$ for RBs and BWs, respectively. We can also estimate the average number density of the CW in the following way. The mass loss rate in the CW can be parameterized as

$$\dot{M}_w = f_w \dot{E} \left(\frac{R_c}{4GM_c} \right) \left(\frac{R_c}{a} \right)^2, \quad (1)$$

where $f_w = 0.1$ is the fraction of the irradiating luminosity intercepted by the companion that goes into launching a thermal wind (I. R. Stevens et al. 1992) and a is the orbital separation between the pulsar and the companion. The number density of the wind is then:

$$n_w(r, \dot{E}) = \frac{\dot{M}_w}{4\pi r^2 v_w m_p}, \quad (2)$$

where r is the distance from the center of the companion, v_w is the escape velocity from the companion and m_p is the proton mass. In order to estimate an upper limit on the wind number density, we calculate n_w at

the companion surface $r = R_2$ for a range of spin-down power $10^{33} - 10^{35} \text{ erg s}^{-1}$. The chosen spin-down power range reflects the variability observed in Tables 2 and 3. Using Eq. 1, we calculate the shock radius according to Eq. B4 in Appendix B. The last relevant quantity is the magnetic field in the companion region, B_c . N. Sanchez & R. W. Romani (2017b) suggest that the companion may have a strong magnetic field; however, this quantity is currently poorly constrained. In this work, we remain agnostic and instead explore a broad range of possible values, $B_c = 0.1 - 10^3 \text{ G}$. All the above-calculated quantities are summarized in Tab. 1.

In the case of protons interacting with the CS, the gamma rays produced are immediately absorbed by the dense companion. The path length of a 1 TeV photon in an environment with number density $\sim 10^{24} \text{ cm}^{-3}$ is $\sim 40 \text{ cm}$. Therefore we find that observable gamma rays are produced exclusively through the interaction of accelerated protons with the CW. In contrast, the majority of the neutrino signal arises from interactions with the CS, due to the significantly higher target proton density. From this point forward, we will calculate gamma rays from proton interactions with the CW and neutrinos from proton interactions with the CS.

4. TRANSPORT EQUATION

In order to calculate the proton spectrum at the interaction site, we consider a simple leaky box model. For both scenarios, we consider a simplified setup in which the particles are injected isotropically from the neutron star. Only those that intersect the interaction regions (displayed in green in Figure 1) are injected into the box and subsequently diffuse away from the pulsar due to the turbulent magnetic field within the box. In case of interaction with the CS, we center the interaction region on the companion. For simplicity, we represent this region as a cylinder, with the normal to the base approximately aligned with the direction of the pulsar wind (see panel (b) of Fig. 1). We set the radius of the cylinder equal to R_c and the height equal to $2R_c$. For interaction with the CW, the interaction occurs in the densest part of the wind, which is located close to the CS. Thus, we model this as a hollow cylinder surrounding the companion, aligned as the previous one. Specifically, we set $R_{\text{inner}} = R_c$ and $R_{\text{outer}} = 2R_c$, and the height equal to $2R_c$ (see panel (a) of Fig. 1). We emphasize that Fig. 1 is provided to illustrate where the interaction takes place. However, the geometrical details do not directly enter our calculation, which depends only on the intersected surface and the length along the axis connecting the pulsar to the CS, along which propagation occurs.

We solve the following transport equation for the number of protons with energy E at a given time t , $N(E, t)$:

$$\frac{\partial N(E, t)}{\partial t} = -\frac{N(E, t)}{\tau_{pp}(E)} - \frac{N(E, t)}{\tau_{esc}(E)} + Q(E, t) \quad (3)$$

where $Q(E, t)$ is the injected proton spectrum, τ_{pp} is the loss timescale due pp interaction with the CW and/or the CS and τ_{esc} is the escape timescale. In particular, τ_{pp} is defined as

$$\tau_{pp}(E) = (n_i c \sigma_{pp})^{-1}, \quad (4)$$

where n_i is the number density of the target i (c: companion or w: companion wind), c is the speed of light and σ_{pp} is the total cross-section of the pp interaction as parameterized by [S. R. Kelner et al. \(2006\)](#). While the escape timescale is

$$\tau_{esc} = \max(\tau_{diff}, \tau_b), \quad (5)$$

where τ_{diff} and τ_b represent the diffusion and ballistic timescales, respectively. We take the maximum of the two to ensure that particles do not diffuse faster than the speed of light. The diffusion timescale, assuming Bohm diffusion, is given by

$$\tau_{diff}(E) = \frac{3R^2}{c} \frac{eB_c}{E}, \quad (6)$$

where B_c is the magnetic field in the companion region (i.e., the downstream region of the IBS), e is the electron charge and R is the size of the box parallel to the direction of propagation of the pulsar wind. We assume that particles are escaping from the base of the cylinders. Thus, $R = 2R_c$ for interactions with both the PW and the CS. The ballistic timescale is

$$\tau_b = \frac{R}{c}. \quad (7)$$

In order to solve Eq. 3, we assume stationarity. This is a reasonable assumption since in the case of millisecond pulsars, the spin-down power remains stable over timescales of \sim Gyr ([D. R. Lorimer & M. Kramer 2004](#)). From Eq. 3, we get:

$$N(E) = Q(E) \tau_{eff}(E) \quad (8)$$

where $\tau_{eff} = (\tau_{pp}^{-1} + \tau_{esc}^{-1})^{-1}$.

For the two considered scenarios, we have two possibilities for the injected proton spectrum: 1) all protons injected with the Lorentz factor of the PW, and 2) protons injected with a power-law spectrum (IBS).

In **scenario 1: PW**, the injected spectrum can be expressed as

$$Q(E, t) = \dot{N}_{GJ}(t) \delta(E - E_{max}(t)), \quad (9)$$

where $\dot{N}_{GJ}(t)$ is the Goldreich-Julian rate defined in Eq. A3 and $E_{max}(t)$ is the energy of the protons flowing with the wind:

$$E_{max}(t) = \Gamma_w m_p c^2, \quad (10)$$

where Γ_w is the wind Lorentz factor. In our model, a large fraction $\eta \sim 1$ of the pulsar spin-down power \dot{E} is converted into kinetic luminosity. In particular, we assume that the luminosity gets distributed among pairs and protons and hence we can write the wind Lorentz factor as ([K. Kotera et al. 2015](#)):

$$\Gamma_w = \frac{\eta \dot{E}}{2k \dot{N}_{GJ} m_e c^2 \left(1 + \frac{m_p}{2k m_e}\right)} \quad (11)$$

where k is the pair multiplicity, namely the number of pairs produced for each electron extracted from the neutron star surface. See Sec. 4.3 for the resulting ranges of Γ_w and E_{max} in spiders.

In **scenario 2: IBS**, the injected spectrum is defined as

$$Q(E, t) = Q_0(t) E^{-\alpha} \exp\left(-\frac{E}{E_{cut}}\right), \quad (12)$$

where $\alpha = 1.5 - 2.5$, E_{cut} is the cut-off energy,

$$Q_0(t) = \frac{\eta_p \dot{E}(t)}{\int_{E_{min}}^{\infty} dE E Q(E, t)} \quad (13)$$

is the normalization factor with η_p being the fraction of the spin-down power that goes into protons. For E_{min} we assume the value 1 GeV (the rest energy of protons). The average post-shock Lorentz factor achievable by particles via magnetic reconnection is $\Gamma \sim \Gamma_w \sigma$ assuming efficient dissipation in the striped pulsar wind. Hence, the cut-off energy is approximately:

$$E_{cut} \simeq \Gamma m_p c^2 = \Gamma_w \sigma m_p c^2 \quad (14)$$

where σ is the magnetization parameter (i.e., the ratio of Poynting to kinetic energy flux). The magnetization in the upstream region of the IBS can be estimated from:

$$\sigma = \frac{B_{sh}^2}{8\pi \Gamma_w (k m_e c^2 + m_p c^2) \rho_{GJ}(R_{sh})} \quad (15)$$

where B_{sh} is the magnetic field in the upstream region of the IBS shock, R_{sh} is the radius of the IBS, $\rho_{GJ}(R_{sh})$ is the Goldreich-Julian density at the IBS location, k is the pair multiplicity, m_e and m_p are the electron and proton mass, respectively. The magnetic field is dipolar inside the pulsar light cylinder $R_{LC} = cP_0/(2\pi)$ with P_0 initial period, and toroidal in the wind, hence:

$$B_{sh} = B_0 \left(\frac{R_{NS}}{R_{LC}}\right)^{-3} \left(\frac{R_{sh}}{R_{LC}}\right)^{-1} \quad (16)$$

where B_0 is the magnetic field at the neutron star surface of a spider system, $R_{\text{NS}} = 10$ km is the radius of the neutron star. The Goldreich-Julian density is calculated accordingly to:

$$\rho_{GJ}(R_{\text{sh}}) = \frac{B_0}{P_0 c e} \left(\frac{R_{\text{LC}}}{R_{\text{sh}}} \right)^2 \quad (17)$$

See Sec. 4.4 for the resulting ranges of σ and E_{cut} in spiders.

4.1. Diffusion vs Advection

In order for the particles that have crossed the IBS to reach the interaction region (depicted in green in Fig. 1), diffusion must be faster than advection within the CW. In other words, the diffusion timescale, $\tau_{\text{diff}}(E) = 3d^2 e B_c / (cE)$, must be shorter than the advection timescale, $\tau_{\text{adv}} = v_w / d$, where $d = a - R_{\text{sh}} - R_c \sim 10^{10}$ cm represents the distance between the IBS and the interaction region. For typical parameters of RBs and BWs (see Tab. 1) we have $v_w \sim 10^7 \text{ cm s}^{-1}$. This comparison sets an upper limit on the magnetic field strength in the companion region, B_c . Ensuring that all protons reach the interaction region is especially crucial for neutrino production, which primarily arises from proton-CS interactions. In contrast, this constraint is more relaxed for gamma rays, as the CW, though less dense, also occupies the region outside the green hollow cylinder in panel (a) of Fig. 1, allowing gamma-ray production in this intermediate region as well.

By comparing the diffusion and advection timescales, we find that protons with $E > 50$ TeV can always manage to reach the CS for the full range of $B_c = 0.1 - 10^3$ G considered in this work. However, protons with $E \sim 10$ TeV can reach the CS only if $B_c \lesssim 170$ G. To ensure efficient neutrino production across the full TeV range, we therefore require $B_c \leq 170$ G. As noted above, this condition is not as strict for gamma rays. In this work, we retain the full range of B_c , since our goal is to identify the parameter ranges that maximize the flux on Earth.

4.2. Timescales

In Fig. 2, we show the timescales as a function of energy, for proton interaction with the CW (panel (a)) and with the CS (panel (b)). In the CW, the escape timescale (Eq. 5) is the shortest and plays the major role while in the CS, the most relevant timescale is the one related to the pp interaction. This is because the companion is very dense, hence, the pp interaction is very fast. In this case (see panel (b)), the uncertainties on the magnetic field don't affect the final results. As we note in Sec. 4.1, it is sufficient that $B_c \leq 170$ G to allow protons to reach the CS. On the other hand, if we focus

on panel (a), we can notice that this uncertainty plays a significant role. The intensity of the magnetic field determines the energy E_{cross} at which $\tau_{\text{diff}} = \tau_b$, marking the transition from diffusive to ballistic propagation. In particular, if the magnetic field is low ($B = 0.1$ G, lower part of the band in Fig. 2), particles with ~ 2 TeV for BWs (~ 5 TeV for RBs) can already escape the box ballistically. Instead, increasing the magnetic field up to 10^3 G shifts this energy up to $> 10^3$ TeV for both BWs and RBs. Additionally, the magnetic field determines the normalization of the proton flux. This is because the intensity of the magnetic field affects how long the particles stay trapped in the box before escaping.

In conclusion, the predicted gamma rays resulting from proton interactions with the CW are subject to significant uncertainties due to the unknown value of the companion's magnetic field. In contrast, neutrinos generated from proton interactions with the CS remain unaffected by this parameter. In the following, we show the effect of variation of B_c on the predicted gamma-ray signal, considering the range $B_c = 0.1 - 10^3$ G.

4.3. Pair multiplicity and fraction of the spin-down power converted into protons

Another uncertain parameter is the pair multiplicity k . In particular, in our model for scenario 1: PW, we consider two possibilities for this value: one based on A. K. Harding & A. G. Muslimov (2011) and a higher value, closer to that typically assumed for pulsars. In A. K. Harding & A. G. Muslimov (2011), the rate of electron and positron pairs in millisecond pulsars was calculated as:

$$\dot{N}_{\text{pair}} = 3.1 \times 10^{34} \text{ s}^{-1} (\dot{E}_{35})^{0.68}, \quad \epsilon = 0.6 \quad (18)$$

where the rate is increased by the presence of an offset polar cap with offset parameter $\epsilon \neq 0$ in the pulsar magnetosphere. Using the above formulas, we calculate the pair multiplicity, $k = \dot{N}_{\text{pair}} / \dot{N}_{\text{GJ}}$, and find that $k = 100$ for $\dot{E} = 10^{33} \text{ erg s}^{-1}$ and $k = 300$ for $\dot{E} = 10^{35} \text{ erg s}^{-1}$. As \dot{E} and the number of pairs increase, the energy available for protons decreases, and vice versa. With these values of k , we estimate that a fraction $\eta_p \sim 0.9 - 0.8$ of the spin-down power is converted into protons, which is quite large. In this regard, we also present results for $k = 10^4$, a higher value for the pair multiplicity, which gives $\eta_p \sim 0.08$.

In the case of scenario 1: PW, the pair multiplicity affects the wind Lorentz factor Γ_w and the maximum proton energy E_{max} defined in Eq. 11 and Eq. 10, respectively. In particular, assuming the multiplicity given by Eq. 18, we obtain a wind Lorentz factor of $\sim 5 \times 10^4$ ($\sim 4.5 \times 10^5$) for a millisecond pulsar with

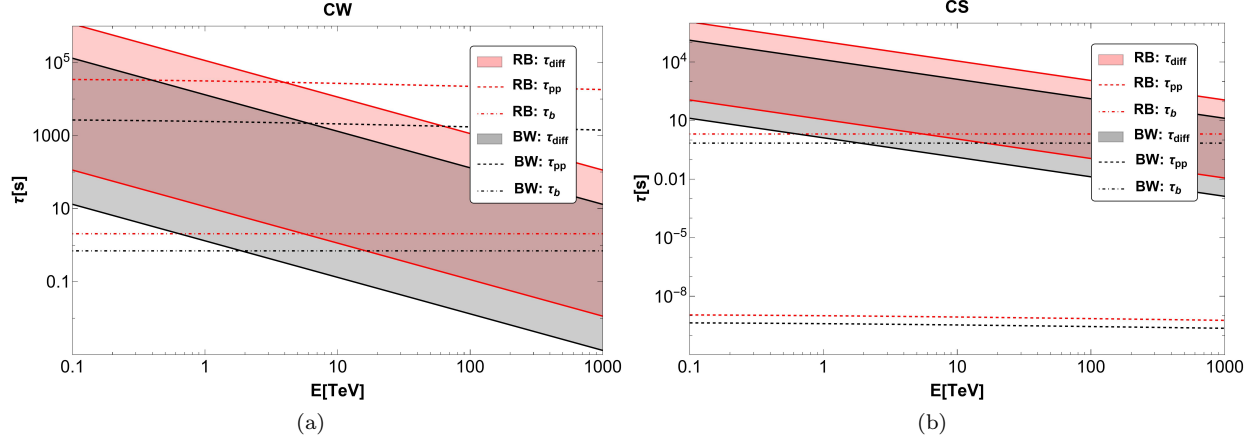


Figure 2. Timescales for the interaction of protons with the CW (panel (a)) and with the CS (panel (b)). The diffusion, pp, and ballistic timescales are displayed with colored-shadowed bands, and dashed, dash-dotted lines, respectively. Timescales for typical RBs (BWs) are displayed in red (black). The uncertainty in τ_{diff} is due to the uncertainty on the magnetic field in the companion region. The lower part of the band is obtained assuming $B_c = 0.1$ G, while the upper part is obtained for $B_c = 10^3$ G.

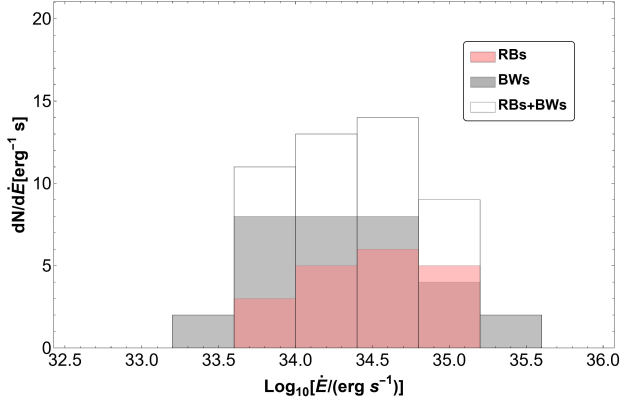


Figure 3. Histogram of the spin-down power for RBs (red), BWs (black), and RBs plus BWs (white) in Tab.2 and Tab.3 with known spin-down power.

spin-down power $\dot{E} = 10^{33} \text{ erg s}^{-1}$ ($\dot{E} = 10^{35} \text{ erg s}^{-1}$), which corresponds to a maximum proton energy of ~ 50 TeV (~ 400 TeV). If we instead consider $k = 10^4$, we get $\Gamma_w \sim 4.9 \times 10^3$ ($\Gamma_w \sim 4.9 \times 10^4$) for a millisecond pulsar with spin-down power $\dot{E} = 10^{33} \text{ erg s}^{-1}$ ($\dot{E} = 10^{35} \text{ erg s}^{-1}$), which corresponds to $E_{\text{max}} = 4.5$ TeV ($E_{\text{max}} = 45$ TeV).

In scenario 1: PW, we treat the multiplicity k as a free parameter, while in scenario 2: IBS, it is more suitable to consider η_p directly as a free parameter. This is because η_p enters the calculation as a pure normalization factor (see Eq. 13) simply scaling our flux predictions up or down.

4.4. Magnetization

To assess the efficiency of magnetic reconnection in accelerating particles in spider systems, we estimate the magnetization parameter σ in the upstream region of the IBS, which is directly related to the cutoff energy (see Eq. 14). By combining Eq. 17, Eq. 16 and Eq. 15 and plugging in typical values for the shock radius $R_{\text{sh}} \sim 10^{11}$ cm, the magnetic field at the neutron star surface $B_0 \sim 10^8$ G and the initial spin period $P_0 \sim 10^{-3}$ s, we obtain magnetization values in the range $\sigma = 0.6 - 6.6$ for $k = 100$ and $\Gamma_w = 10^4 - 10^5$, and $\sigma = 0.06 - 0.6$ for $k = 10^4$ and the same range of the wind Lorentz factor. These parameters yield average post-shock Lorentz factors of $\Gamma \sim 10^5$ for $k = 100$ and $\Gamma \sim 10^4$ for $k = 10^4$. Assuming protons, the corresponding average particle energies are ~ 60 TeV and ~ 6 TeV for $\Gamma = 10^5$ and $\Gamma = 10^4$, respectively. In this work, we adopt $E_{\text{cut}} = 60$ TeV, the maximum predicted value, as our standard reference case, as we aim to consider the most optimistic scenario for gamma-ray and neutrino detection. It is important to note that E_{cut} remains somewhat uncertain, as it depends on the acceleration mechanism and poorly constrained parameters such as B_{sh} .

The estimated range of σ is consistent with what is assumed in the simulation by J. Cortés & L. Sironi (2024), who adopt $\sigma = 10$. In our case, the magnetization is lower due to the inclusion of protons (see Eq. 15). In the absence of protons, we obtain $\sigma = 6.7 - 67$ for $k = 100$.

The post-shock magnetic field value is uncertain, and therefore we assume a broad range $0.1 - 10^3$ G. This

leads to a downstream magnetization $\sigma \ll 10^{-3}$ that is compatible with what is required by observations (see C. J. T. van der Merwe et al. 2020). In this framework, nearly all the magnetic energy is converted into particle kinetic energy; hence, we can fairly assume $\eta \sim 1$.

5. GAMMA-RAY AND NEUTRINO FLUX

We use the result of the above sections to calculate the gamma-ray flux at Earth:

$$\phi_\gamma = \frac{cn_i}{4\pi d^2} \left(\frac{S_i}{S_{\text{tot}}} \right) \int_{E_\gamma}^{\infty} dE \frac{d\sigma(E, E_\gamma)}{dE_\gamma} N(E) \quad (19)$$

where $N(E)$ is defined in Eq. 8, $d\sigma(E, E_\gamma)/dE_\gamma$ represents the differential cross section for the production of photons by a nucleon of energy E in a nucleon-nucleon collision, parameterized as in S. R. Kelner et al. (2006), n_i is the number density of the wind or the companion and d is the distance of the considered spider source from Earth. The gamma-ray flux is rescaled by a factor S_i/S_{tot} . Since the protons are assumed to be emitted isotropically from the neutron star surface, only a fraction of these protons will intercept the target material. We define the intercepted surface as S_i and the total surface as $S_{\text{tot}} = 4\pi a^2$. In particular, $S_i = \pi R_c^2$ in case of interaction with the CS, while $S_i = \pi(4R_c)^2 - \pi R_c^2 = 3\pi R_c^2$ in case of interaction with the CW. Analogously, we calculate the all-flavor neutrino flux as:

$$\phi_\nu = \frac{cn_i}{4\pi d^2} \left(\frac{S_i}{S_{\text{tot}}} \right) \sum_{l=e,\mu,\tau} \int_{E_\nu}^{\infty} dE \frac{d\sigma_l(E, E_\nu)}{dE_\nu} N(E) \quad (20)$$

where $\frac{d\sigma_l(E, E_\nu)}{dE_\nu}$ represents the differential cross section for the production of a neutrino and antineutrino with flavor l by a nucleon of energy E in a nucleon-nucleon collision (S. R. Kelner et al. 2006).

6. SYNTHETIC POPULATION OF SPIDERS

In the final part of this work, we evaluate the contribution of a synthetic population of spiders to the Galactic diffuse emission. In the following, we perform this calculation only for neutrinos. The gamma-ray diffuse emission measured at very-high energy by LHAASO-KM2A (Z. Cao et al. 2023) has already been shown to be well explained by hadronic diffuse emission alone, without requiring a significant contribution from unresolved sources (V. Vecchiotti et al. 2024).

In order to estimate the contribution of the entire spider population to the Galactic neutrino flux, we build a synthetic population of these systems. For each source, we extract the location in the Galaxy and the spin-down

power. In particular, we assume that the spatial distribution is proportional to the Lorimer distribution (D. R. Lorimer et al. 2006) expressed in cylindrical coordinates:

$$n_s(\rho, z) = n_{\text{loc}} \left(\frac{\rho}{\rho_\odot} \right)^{1.9} \exp \left(-b \frac{\rho - \rho_\odot}{\rho_\odot} \right) \exp \left(-\frac{z}{z_e} \right) \quad (21)$$

where $\rho_\odot = 8.5$ kpc is the distance of the Sun from the Galactic center, $b = 5$ and $z_e = 0.5$ kpc (M. Linares & M. Kachelriess 2021). The distribution is normalized to the local number of spiders n_{loc} . This last value is conservatively estimated by assuming that all spiders within a cylinder of 1 kpc radius have already been detected. We adopt the value obtained in M. Linares & M. Kachelriess (2021), $n_{\text{loc}} \sim 7 \text{ kpc}^{-3}$, as a normalization factor.

The other parameter of our simulation is the spin-down power. The histogram of \dot{E} derived using the sample of known spiders (listed in Tab. 2 and Tab. 3) is reported in Fig. 3. In general, we expect to be able to detect only the brightest sources, hence the ones that have the highest \dot{E} . Based on Fig. 3, we consider two possibilities for the logarithmic distribution of the spin-down power. The first simple case is a uniform logarithmic distribution for both RBs and BWs. In order to do so, we extract uniformly a value in the interval $v = [33, 35]$ and calculate the spin-down power as 10^v . The second possibility is to parameterize the logarithmic distribution of \dot{E} as a Gaussian with mean fixed to $\mu = 34.5$ and variance $\sigma = 0.5$. Apart from the location and the spin-down power, all the other parameters are kept constant since they don't strongly affect the final neutrino flux. We consider 3 cases for scenario 1 (PW→CS(ν)) to account for all possible underlying populations and values of the pair multiplicity k :

- a) All sources are RB and the pair multiplicity is calculated according to Eq. 18. However, this is a conceptual scenario we consider to maximize the neutrino flux, but it doesn't hold up in reality;
- b) Half of the sources are RBs, and the other half are BWs. The pair multiplicity is calculated according to Eq. 18;
- c) Half of the sources are RBs, and the other half are BWs. The pair multiplicity is fixed to $k = 10^4$;

For each case, we simulate 100 populations where each population has an average number of ~ 3600 spiders, obtained by integrating the spatial distribution in the region $|l| < 180^\circ$ and $|b| < 5^\circ$, where IceCube reported the measurement of the Galactic diffuse neutrino emission (R. Abbasi et al. 2023).

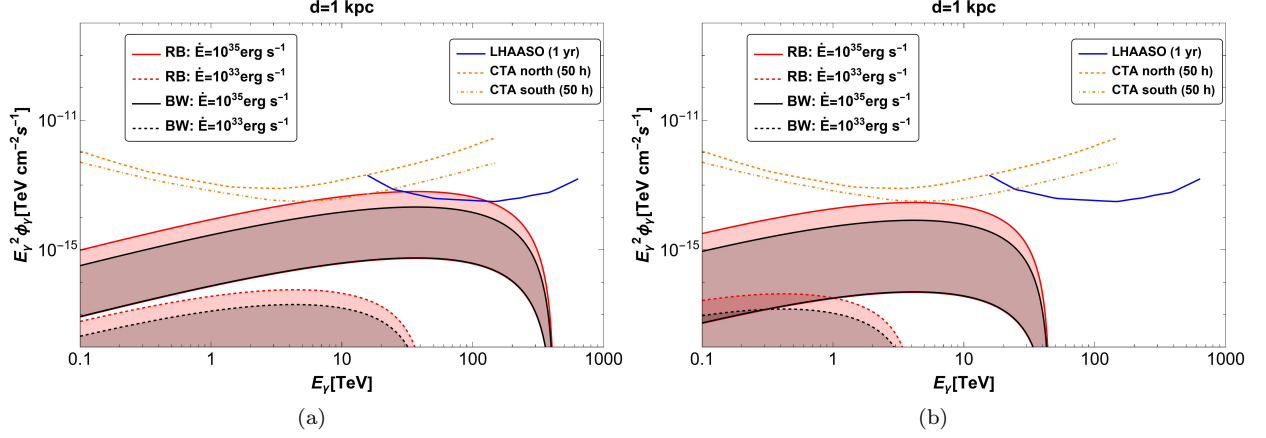


Figure 4. Scenario 1: PW→CW(γ) Maximum (panel (a)) and minimum (panel (b)) gamma-ray flux from a typical RB (red bands) and BW (black bands). All the curves are calculated assuming that protons are injected as a delta function. The solid (dashed) lines are obtained for $\dot{E} = 10^{35} \text{ erg s}^{-1}$ ($\dot{E} = 10^{33} \text{ erg s}^{-1}$). The bands include the uncertainty on the magnetic field in the companion region B_c . The upper (lower) bound is obtained assuming $B_c = 10^3 \text{ G}$ ($B_c = 0.1 \text{ G}$). The maximum is obtained by calculating the multiplicity according to Eq. 18. The minimum is obtained assuming a fixed multiplicity of 10^4 . The dashed and dot-dashed orange lines represent the 50 h CTA sensitivity in the north and south hemispheres, respectively (S. Celli & G. Peron 2024). The blue solid line represents the 1 year LHAASO sensitivity (S. Celli & G. Peron 2024).

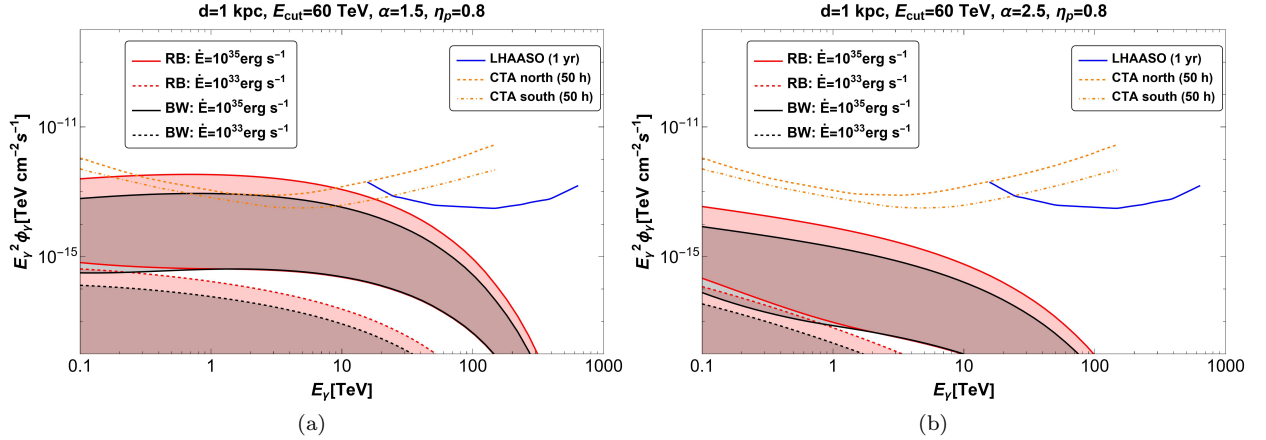


Figure 5. Scenario 2: IBS→CW(γ) Maximum for gamma-ray flux from a typical RB (red lines) and BW (black lines). All the curves are calculated assuming $\eta_p = 0.8$ and that protons are injected as a power-law with an exponential cut-off, where the spectral index is fixed to $\alpha = 1.5$ (panel (a)) and $\alpha = 2.5$ (panel (b)) and the cut-off energy is fixed to 60 TeV, calculated according to Eq. 14. The bands include the uncertainty on the magnetic field in the companion region B_c . The upper (lower) bound is obtained assuming $B_c = 10^3 \text{ G}$ ($B_c = 0.1 \text{ G}$).

7. RESULTS

7.1. Generic single spiders

Using typical values for RBs and BWs, as listed in Tab. 1, we calculate the gamma-ray and the neutrino emission produced by the interaction of protons with the CW and the CS, respectively. We predict the fluxes for the two proton acceleration scenarios considered in this work (PW and IBS).

In Figures 4 and 6, we show the gamma-ray and all-flavor neutrino flux in the case of scenario 1 (PW), for two different assumptions on the spin-down power: $\dot{E} = 10^{33} \text{ erg s}^{-1}$ (dashed lines) and $\dot{E} = 10^{35} \text{ erg s}^{-1}$ (solid lines). All the curves are calculated assuming that protons are injected as a delta function, with the predicted maximum achievable flux displayed in panel (a) and the minimum in panel (b). In particular, the maximum for the gamma-ray and neutrino fluxes is obtained by calculating the pair multiplicity k according to

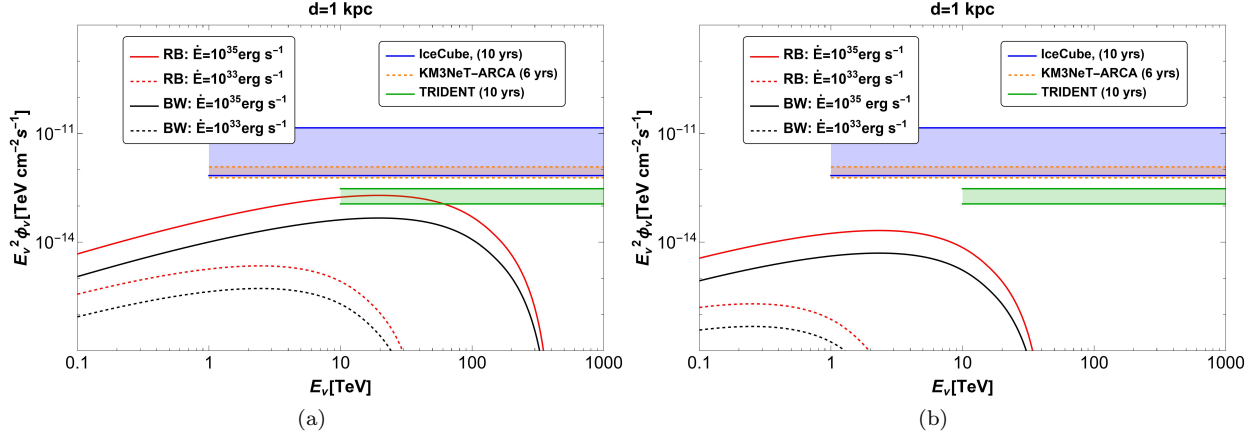


Figure 6. Scenario 1: $\text{PW} \rightarrow \text{CS}(\nu)$ Same as in Fig. 4 but for the all-flavor neutrino flux. The 90% confidence-level median sensitivities of the IceCube (blue band) (M. G. Aartsen et al. 2020), KM3Net-ARCA (orange band) (S. Aiello et al. 2019), and TRIDENT (green band) (Z. P. Ye et al. 2023) detectors, based on 10, 6, and 10 years of data taking, respectively, are shown assuming a power-law source spectrum with an index of 2. The exact sensitivity value will depend on the declination of the considered source.

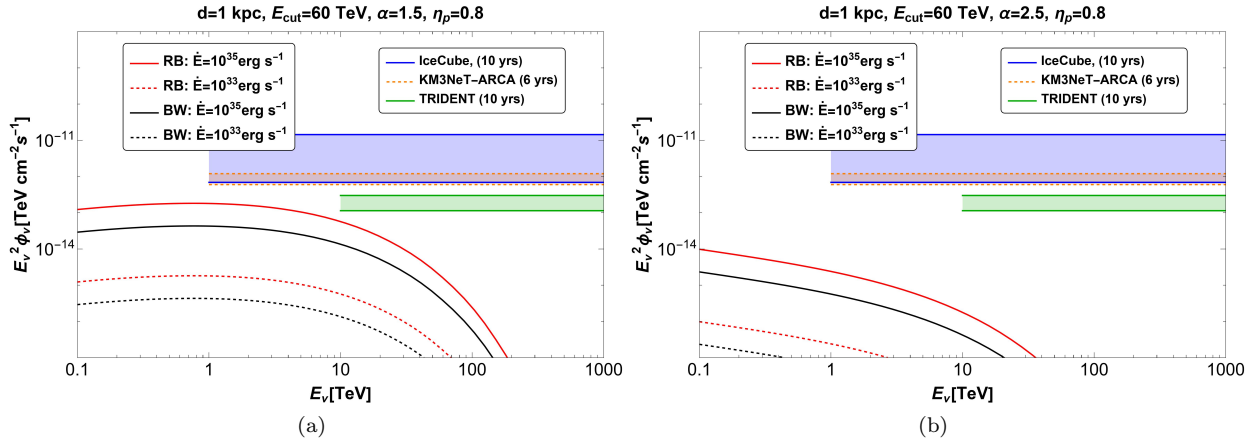


Figure 7. Scenario 2: $\text{IBS} \rightarrow \text{CS}(\nu)$ Same as in Fig. 5 but for the all-flavor neutrino flux. The 90% confidence-level median sensitivities of the IceCube (blue band) (M. G. Aartsen et al. 2020), KM3Net-ARCA (orange band) (S. Aiello et al. 2019), and TRIDENT (green band) (Z. P. Ye et al. 2023) detectors, based on 10, 6, and 10 years of data taking, respectively, are shown assuming a power-law source spectrum with an index of 2.

Eq. 18. The minimum flux is instead obtained assuming a fixed pair multiplicity of 10^4 .

We display our prediction for the gamma-ray and all-flavor neutrino in the case of scenario 2 (IBS) in Figures 5 and 7, respectively. All the curves are calculated assuming that protons are injected as a power-law with an exponential cut-off. The spectral index is fixed to $\alpha = 1.5$ in panel (a) and $\alpha = 2.5$ in panel (b), while the cut-off energy is fixed at 60 TeV, as calculated from Eq. 14 for the highest magnetization σ achievable in our model. We have also fixed the fraction of spin-down power transferred to protons to the maximum $\eta_p = 0.8$. For scenario 2 (IBS), we chose to display only our pre-

diction for the maximum flux, since changing η_p in this case simply rescales the normalization without affecting the maximum achievable energy, which is instead determined by the magnetization in the upstream region of the IBS.

Looking at Figures 4 and 5, we notice that, for specific parameter combinations, a spider system could produce a gamma-ray flux that is above the sensitivity threshold of CTA (orange lines) and LHAASO (blue line) (S. Celli & G. Peron 2024). In particular, in scenario 1 (PW) for a RB-like system, if the spider has a spin-down power of $\dot{E} = 10^{35} \text{ erg s}^{-1}$ and it is located at a distance $d = 1 \text{ kpc}$ from the Sun, the source could be de-

tected by both LHAASO and CTA, provided the magnetic field in the companion region is sufficiently high and the multiplicity is sufficiently low (see panel (a) of Fig. 4). However, if the multiplicity is fixed to 10^4 , the source would barely be detectable by CTA (see panel (b) of Fig. 4), assuming the same spin-down power and high magnetic field. Spiders at distances shorter than 1 kpc would have higher gamma-ray fluxes (e.g., the RB candidate 3FGL J0737.2-3233 at $d = 0.66 \pm 0.02$ kpc, [M. Turchetta et al. 2024](#)).

In scenario 2 (IBS), the requirements for detecting a RB-like system in terms of spin-down power and magnetic field are similar to those in scenario 1 (PW). In the most optimistic case with $\eta_p = 0.8$ and $\alpha = 1.5$, the signal exceeds only the detection thresholds of CTA. This is due to the cut-off energy of the injected spectrum, which is fixed at 60 TeV; as a result, most of the gamma rays are produced within the CTA energy range, rather than that of LHAASO KM2A. It is also important to note that for lower values of the magnetization σ , the resulting cut-off energy would be lower, making detection with the LHAASO-KM2A detector unlikely. The injected spectral index is also a crucial parameter. In fact, if the injected proton spectrum is too soft, for example, such as with $\alpha = 2.5$ (as shown in panel (b) of Fig. 5), the IBS-CW signal would always remain below the detection threshold.

In general, the main caveat of above considerations is that, for low values of the pair multiplicity k (in scenario 1: PW) and low values of the fraction of spin-down power transferred to protons η_p (in scenario 2: IBS), spider sources are unlikely to produce a detectable signal via the two suggested scenarios for current and upcoming gamma-ray detectors.

In the neutrino case (see Fig. 6), a nearby spider system could produce a flux above the upcoming TRIDENT (green band) ([Z. P. Ye et al. 2023](#)) detectors in Scenario 1 (PW-CS) for the most optimistic case (see panel (a) of Fig. 6). In the case of scenario 2 (IBS-CS), shown in Fig. 7, no individual system produces a detectable signal for all the considered values of α . This is mainly due to the lower cut-off in the proton energy, $E_{\text{cut}} = 60$ TeV, compared to scenario 1, which results in a cut-off in the neutrino energy at $\sim \text{few}$ TeV. Although it seems challenging to detect the neutrino signal from single spiders, the cumulative neutrino signal produced by all the spider systems in our Galaxy could provide a non-negligible contribution to the measured IceCube signal. In the following, we quantify this contribution.

7.2. Sample of known spiders

For the most optimistic scenario 1 (PW) and assuming k from Eq. 18 to maximize the flux, we calculate the gamma-ray and neutrino flux from a sample of known spiders with measured distance and spin-down power. The sample considered includes 19 RBs and 32 BWs, which constitute the subset of systems for which we have information on the dispersion measure distance d_{DM} and spin-down power \dot{E} , as reported in Tables 2 and 3 ([I. F. Nedreaas 2024](#)).

The results of our calculation are shown in Figures 8 and 9 for gamma-rays and neutrinos, respectively. In particular, panel (a) of Fig. 8, displays the results assuming a companion magnetic field of 10 G, while panel (b), shows the result for a companion magnetic field of 10^3 G. As noted in Sec. 4.2, this parameter plays a crucial role in gamma-ray predictions. A high value of B_c could make some spider systems detectable by LHAASO and the upcoming CTA. This is especially true for two RB systems, PSR J1910-5320 and PSR J1723-2837, which appear to produce a signal above the LHAASO sensitivity threshold (see panel (b) of Fig. 8). These are two nearby sources ($d_{\text{DM}} \leq 1$ kpc) with high spin-down powers of $\sim 10^{35} \text{ erg s}^{-1}$. A counterpart for PSR J1910-5320 has been identified in the 4FGL catalog ([S. Abdollahi et al. 2020](#)), precisely the Fermi-LAT sources 4FGL J1910.7-5320 ([K.-Y. Au et al. 2023](#); [O. G. Dodge et al. 2024](#)). PSR J1723-2837, on the other hand, shows some hint of gamma-rays, as reported by [C. Y. Hui et al. \(2014\)](#) and [C. J. T. van der Merwe et al. \(2020\)](#). However, the LHAASO collaboration, in their first catalog based on 508 days of data collected by the Water Cherenkov Detector Array (WCDA) and the Kilometer Squared Array (KM2A), has not yet reported any significant detections from the locations of these two systems ([Z. Cao et al. 2024](#)). This measurement does not exclude the possibility that, with more data, it may still be possible to detect these spiders. In general, for the above-mentioned systems, we can set an upper limit on the magnetic field in the companion region: it must be $< 10^3$ G.

Regarding neutrinos (see Fig. 9), none of the currently known spiders are expected to produce a detectable signal for IceCube ([M. G. Aartsen et al. 2020](#)) or the KM3NeT-ARCA ([S. Aiello et al. 2019](#)). However, the future TRIDENT detector ([Z. P. Ye et al. 2023](#)), with its improved sensitivity, could potentially detect neutrino emission from a group of spider sources, particularly RBs. In general, it is worthwhile to investigate the contribution of the cumulative neutrino flux from a synthetic population of spider sources to the currently measured diffuse neutrino emission ([R. Abbasi et al. 2023](#)).

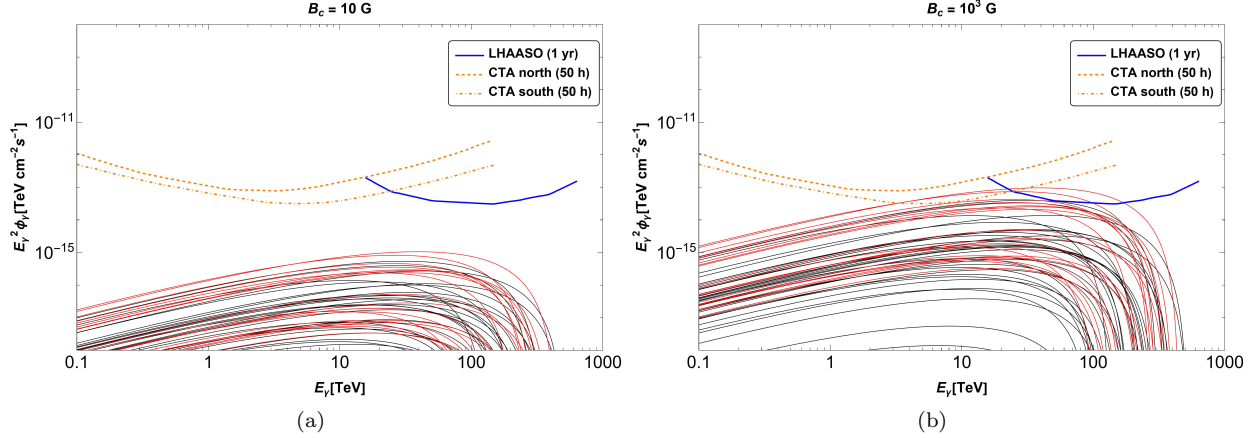


Figure 8. Panel (a): Gamma-ray flux from known RBs (red thin lines) and BWs (black thin lines), listed in Tab. 2 and Tab. 3, respectively. The flux is calculated assuming a companion magnetic field fixed at $B_c = 10$ G. We also display the LHAASO 1 yr sensitivity threshold (blue line) and the 50 h CTA sensitivity threshold (orange lines). Panel (b): Same as panel (a) but with companion magnetic field fixed at $B_c = 10^3$ G. All the curves are calculated assuming scenario 1 with k calculated from Eq. 18.

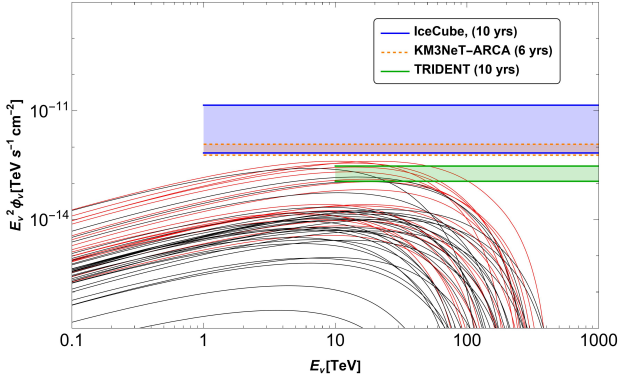


Figure 9. All-flavour neutrino flux from known RBs (red thin lines) and BWs (black thin lines). We also display the 10 yrs IceCube (blue line) and KM3Net (dashed orange line) sensitivity threshold. All the curves are calculated assuming scenario 1 with k calculated from Eq. 18.

7.3. Cumulative neutrino flux

In Fig. 10, we show the total neutrino flux produced by our synthetic population of spiders for the 3 cases listed in Sec. 6 in the sky region: $|l| \leq 180^\circ$ and $|b| \leq 5^\circ$. The total flux is calculated as the median value over 100 realizations. We present the median value instead of the average to reduce the impact of large fluctuations, which can arise in some realizations due to the occasional presence of a powerful source located near the Sun. The dashed lines are calculated assuming that $\log_{10} \dot{E}$ is distributed uniformly, while the solid lines are obtained assuming a Gaussian distribution. The former possibility produces slightly lower fluxes with respect to the latter one.

Our predictions for Case a) are displayed with red lines. This case, though unrealistic, produces the largest

neutrino flux. Indeed, the total neutrino flux from the spider population calculated assuming a $\log_{10} \dot{E}$ Gaussian (uniform) distribution can contribute up to 5–16% (2–6%) to the IceCube diffuse emission flux at 20 TeV (R. Abbasi et al. (2023)). In Case b) (see blue lines), obtained by considering a combined population of RBs and BWs, the percentage decreases to 3–10% (1–3%).

Lastly, in Case c) (see cyan lines), with $k = 10^4$ and consequently $\eta_p \sim 0.08$, it produces a neutrino flux that is a few orders of magnitude below the level of the Galactic diffuse emission measured by IceCube (R. Abbasi et al. (2023)).

In general, including BWs in the spider population has the effect of slightly decreasing both the maximum achievable energy and the total flux. Increasing the multiplicity k , as already noted in Sec. 4.3, has the same effect in a more drastic way.

In conclusion, we find that the total population of spiders gives a negligible contribution to the total galactic neutrino flux measured by IceCube.

8. CONCLUSIONS

In this paper, we have calculated the very high-energy (0.1–10³ TeV) gamma-ray and neutrino emission in spider systems, produced by protons accelerated at the IBS and/or within the PW as they interact with the CW and the CS. We have shown that the interaction between the IBS and CW can produce detectable gamma-ray emission at ~ 1 TeV for CTA, but only if the injected proton spectrum at the shock is hard ($\alpha = 1.5$) and the companion's magnetic field is sufficiently strong ($\sim 10^3$ G). We also find that the interaction between the IBS and CS is unlikely to generate any detectable neutrino emission. On the other hand, the interaction between the PW and

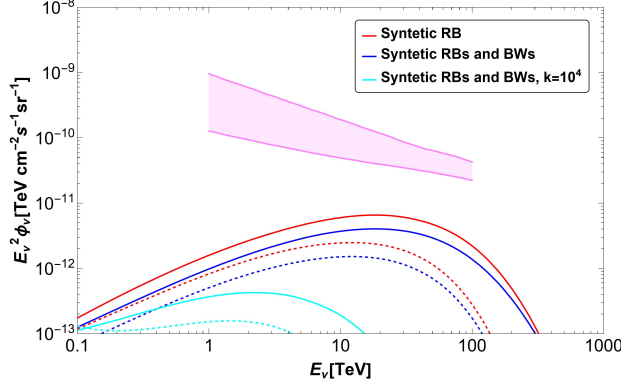


Figure 10. Differential energy spectra of the all-flavor neutrino flux from a population of spiders, all RBs (red lines), half RBs and half BWs (blue lines), half RBs and half BWs with pair multiplicity $k = 10^4$ (cyan lines) in the sky region $|l| \leq 180^\circ$ and $|b| \leq 5^\circ$. Solid lines are obtained by extracting $\log_{10} \dot{E}$ from a Gaussian distribution with mean $\mu = 34.5$ and variance $\sigma = 0.5$. Dashed lines are obtained by extracting $\log_{10} \dot{E}$ from a uniform distribution in the interval $[33, 35]$. The magenta region corresponds to the superposition of the three IceCube best-fits for the galactic component with their 1σ uncertainty (R. Abbasi et al. 2023).

CW may produce a detectable gamma-ray signal at a few TeV (CTA) and possibly at ~ 100 TeV (LHAASO), provided the pair multiplicity is low ($k \sim 100$ – 300). Regarding neutrinos, the interaction between the PW and CS could lead to detectable neutrino emission for the future TRIDENT detector (Z. P. Ye et al. 2023), again assuming a low pair multiplicity. Finally, we have estimated the contribution of a synthetic population of spiders to the diffuse neutrino flux recently measured by IceCube (R. Abbasi et al. 2023), showing that this contribution is negligible.

ACKNOWLEDGMENTS

The authors are grateful to Alice K. Harding, Elena Amato, and Benedikt Schroer for their helpful discussions and comments. The work of VV and ML is supported by the European Research Council (ERC) under the ERC-2020-COG ERC Consolidator Grant (Grant agreement No.101002352).

REFERENCES

- Aartsen, M. G., et al. 2020, Phys. Rev. Lett., 124, 051103, doi: [10.1103/PhysRevLett.124.051103](https://doi.org/10.1103/PhysRevLett.124.051103)
- Abbasi, R., Ackermann, M., Adams, J., et al. 2023, Science, 380, 1338, doi: [10.1126/science.adc9818](https://doi.org/10.1126/science.adc9818)
- Abdollahi, S., et al. 2020, Astrophys. J. Suppl., 247, 33, doi: [10.3847/1538-4365/ab6bcb](https://doi.org/10.3847/1538-4365/ab6bcb)
- Aiello, S., et al. 2019, Astropart. Phys., 111, 100, doi: [10.1016/j.astropartphys.2019.04.002](https://doi.org/10.1016/j.astropartphys.2019.04.002)
- Amato, E., Guetta, D., & Blasi, P. 2003, A&A, 402, 827, doi: [10.1051/0004-6361:20030279](https://doi.org/10.1051/0004-6361:20030279)
- An, H., Romani, R. W., & Kerr, M. 2018, The Astrophysical Journal Letters, 868, L8, doi: [10.3847/2041-8213/aaedaf](https://doi.org/10.3847/2041-8213/aaedaf)
- An, H., Romani, R. W., & Kerr, M. 2020, Astrophys. J., 897, 52, doi: [10.3847/1538-4357/ab93ba](https://doi.org/10.3847/1538-4357/ab93ba)
- Arons, J., & Tavani, M. 1993, ApJ, 403, 249, doi: [10.1086/172198](https://doi.org/10.1086/172198)
- Au, K.-Y., et al. 2023, Astrophys. J., 943, 103, doi: [10.3847/1538-4357/aca8a8](https://doi.org/10.3847/1538-4357/aca8a8)
- Bogdanov, S., Archibald, A. M., Hessels, J. W. T., et al. 2011, The Astrophysical Journal, 742, 97, doi: [10.1088/0004-637X/742/2/97](https://doi.org/10.1088/0004-637X/742/2/97)
- Bogdanov, S., Bahramian, A., Heinke, C. O., et al. 2021, The Astrophysical Journal, 912, 124, doi: [10.3847/1538-4357/abee78](https://doi.org/10.3847/1538-4357/abee78)
- Bogdanov, S., Grindlay, J. E., & van den Berg, M. 2005, The Astrophysical Journal, 630, 1029, doi: [10.1086/432249](https://doi.org/10.1086/432249)
- Bogovalov, S. V. 1999, Astron. Astrophys., 349, 1017, <https://arxiv.org/abs/astro-ph/9907051>
- Cao, Z., et al. 2023, Phys. Rev. Lett., 131, 151001, doi: [10.1103/PhysRevLett.131.151001](https://doi.org/10.1103/PhysRevLett.131.151001)
- Cao, Z., et al. 2024, Astrophys. J. Suppl., 271, 25, doi: [10.3847/1538-4365/acfd29](https://doi.org/10.3847/1538-4365/acfd29)
- Celli, S., & Peron, G. 2024, Astron. Astrophys., 689, A258, doi: [10.1051/0004-6361/202449837](https://doi.org/10.1051/0004-6361/202449837)
- Clark, C. J., et al. 2021, Mon. Not. Roy. Astron. Soc., 502, 915, doi: [10.1093/mnras/staa3484](https://doi.org/10.1093/mnras/staa3484)
- Clark, C. J., et al. 2023, Nature Astron., 7, 451, doi: [10.1038/s41550-022-01874-x](https://doi.org/10.1038/s41550-022-01874-x)
- Corbet, R. H. D., et al. 2022, Astrophys. J., 935, 2, doi: [10.3847/1538-4357/ac6fe2](https://doi.org/10.3847/1538-4357/ac6fe2)
- Cortés, J., & Sironi, L. 2022, Astrophys. J., 933, 140, doi: [10.3847/1538-4357/ac74b2](https://doi.org/10.3847/1538-4357/ac74b2)
- Cortés, J., & Sironi, L. 2024, Mon. Not. Roy. Astron. Soc., 534, 2551, doi: [10.1093/mnras/stae2278](https://doi.org/10.1093/mnras/stae2278)
- Cortés, J., & Sironi, L. 2025, <https://arxiv.org/abs/2501.08387>
- Dodge, O. G., et al. 2024, Mon. Not. Roy. Astron. Soc., 528, 4337, doi: [10.1093/mnras/stae211](https://doi.org/10.1093/mnras/stae211)

- Gallant, Y. A., & Arons, J. 1994, *ApJ*, 435, 230, doi: [10.1086/174810](https://doi.org/10.1086/174810)
- Gentile, P. A., Roberts, M. S. E., McLaughlin, M. A., et al. 2014, *ApJ*, 783, 69, doi: [10.1088/0004-637X/783/2/69](https://doi.org/10.1088/0004-637X/783/2/69)
- Guépin, C., Cerutti, B., & Kotera, K. 2020, *Astron. Astrophys.*, 635, A138, doi: [10.1051/0004-6361/201936816](https://doi.org/10.1051/0004-6361/201936816)
- Harding, A. K., & Gaisser, T. K. 1990, *ApJ*, 358, 561, doi: [10.1086/169009](https://doi.org/10.1086/169009)
- Harding, A. K., & Muslimov, A. G. 2011, *ApJ*, 743, 181, doi: [10.1088/0004-637X/743/2/181](https://doi.org/10.1088/0004-637X/743/2/181)
- Hoshino, M., Arons, J., Gallant, Y. A., & Langdon, A. B. 1992, *ApJ*, 390, 454, doi: [10.1086/171296](https://doi.org/10.1086/171296)
- Huang, R. H. H., Kong, A. K. H., Takata, J., et al. 2012, *The Astrophysical Journal*, 760, 92, doi: [10.1088/0004-637X/760/1/92](https://doi.org/10.1088/0004-637X/760/1/92)
- Hui, C. Y., Tam, P. H. T., Takata, J., et al. 2014, *Astrophys. J. Lett.*, 781, L21, doi: [10.1088/2041-8205/781/1/L21](https://doi.org/10.1088/2041-8205/781/1/L21)
- Kandel, D., Romani, R. W., & An, H. 2019, *The Astrophysical Journal*, 879, 73, doi: [10.3847/1538-4357/ab24d9](https://doi.org/10.3847/1538-4357/ab24d9)
- Kandel, D., Romani, R. W., & An, H. 2021, *ApJL*, 917, L13, doi: [10.3847/2041-8213/ac15f7](https://doi.org/10.3847/2041-8213/ac15f7)
- Kelner, S. R., Aharonian, F. A., & Bugayov, V. V. 2006, *Phys. Rev. D*, 74, 034018, doi: [10.1103/PhysRevD.74.034018](https://doi.org/10.1103/PhysRevD.74.034018)
- Kotera, K., Amato, E., & Blasi, P. 2015, *JCAP*, 08, 026, doi: [10.1088/1475-7516/2015/08/026](https://doi.org/10.1088/1475-7516/2015/08/026)
- Lattimer, J. M., & Prakash, M. 2007, *Phys. Rept.*, 442, 109, doi: [10.1016/j.physrep.2007.02.003](https://doi.org/10.1016/j.physrep.2007.02.003)
- Lemoine, M., Kotera, K., & Pétri, J. 2015, *JCAP*, 07, 016, doi: [10.1088/1475-7516/2015/07/016](https://doi.org/10.1088/1475-7516/2015/07/016)
- Linares, M. 2014, *Astrophys. J.*, 795, 72, doi: [10.1088/0004-637X/795/1/72](https://doi.org/10.1088/0004-637X/795/1/72)
- Linares, M., & Kachelriess, M. 2021, *JCAP*, 02, 030, doi: [10.1088/1475-7516/2021/02/030](https://doi.org/10.1088/1475-7516/2021/02/030)
- Lorimer, D. R., & Kramer, M. 2004, *Handbook of Pulsar Astronomy*, Vol. 4
- Lorimer, D. R., Faulkner, A. J., Lyne, A. G., et al. 2006, *Mon. Not. Roy. Astron. Soc.*, 372, 777, doi: [10.1111/j.1365-2966.2006.10887.x](https://doi.org/10.1111/j.1365-2966.2006.10887.x)
- Nedreaas, I. F. 2024, <https://hdl.handle.net/11250/3143780>
- Ng, C. W., Takata, J., Strader, J., Li, K. L., & Cheng, K. S. 2018, *The Astrophysical Journal*, 867, 90, doi: [10.3847/1538-4357/aae308](https://doi.org/10.3847/1538-4357/aae308)
- Petri, J., & Lyubarsky, Y. 2008, *Int. J. Mod. Phys. D*, 17, 1961, doi: [10.1142/S0218271808013637](https://doi.org/10.1142/S0218271808013637)
- Philippov, A., Timokhin, A., & Spitkovsky, A. 2020, *Phys. Rev. Lett.*, 124, 245101, doi: [10.1103/PhysRevLett.124.245101](https://doi.org/10.1103/PhysRevLett.124.245101)
- Philippov, A. A., & Spitkovsky, A. 2018, *Astrophys. J.*, 855, 94, doi: [10.3847/1538-4357/aaabbc](https://doi.org/10.3847/1538-4357/aaabbc)
- Romani, R. W., & Sanchez, N. 2016, *ApJ*, 828, 7, doi: [10.3847/0004-637X/828/1/7](https://doi.org/10.3847/0004-637X/828/1/7)
- Sanchez, N., & Romani, R. W. 2017a, *The Astrophysical Journal*, 845, 42, doi: [10.3847/1538-4357/aa7a02](https://doi.org/10.3847/1538-4357/aa7a02)
- Sanchez, N., & Romani, R. W. 2017b, *Astrophys. J.*, 845, 42, doi: [10.3847/1538-4357/aa7a02](https://doi.org/10.3847/1538-4357/aa7a02)
- Sim, M., An, H., & Wadiasingh, Z. 2024, *Astrophys. J.*, 964, 109, doi: [10.3847/1538-4357/ad25fb](https://doi.org/10.3847/1538-4357/ad25fb)
- Sironi, L., Keshet, U., & Lemoine, M. 2015, *Space Sci. Rev.*, 191, 519, doi: [10.1007/s11214-015-0181-8](https://doi.org/10.1007/s11214-015-0181-8)
- Smith, D. A., Abdollahi, S., Ajello, M., et al. 2023, *The Astrophysical Journal*, 958, 191, doi: [10.3847/1538-4357/acee67](https://doi.org/10.3847/1538-4357/acee67)
- Stevens, I. R., Rees, M. J., & Podsiadlowski, P. 1992, *Monthly Notices of the Royal Astronomical Society*, 254, 19P, doi: [10.1093/mnras/254.1.19P](https://doi.org/10.1093/mnras/254.1.19P)
- Strader, J., et al. 2019, *Astrophys. J.*, 872, 42, doi: [10.3847/1538-4357/aafbaa](https://doi.org/10.3847/1538-4357/aafbaa)
- Turchetta, M., Linares, M., Koljonen, K., et al. 2024, *ApJ*, 977, 65, doi: [10.3847/1538-4357/ad89a3](https://doi.org/10.3847/1538-4357/ad89a3)
- van der Merwe, C. J. T., Wadiasingh, Z., Venter, C., Harding, A. K., & Baring, M. G. 2020, *ApJ*, 904, 91, doi: [10.3847/1538-4357/abdbfb](https://doi.org/10.3847/1538-4357/abdbfb)
- Vecchiotti, V., Peron, G., Amato, E., et al. 2024, <https://arxiv.org/abs/2411.11439>
- Wadiasingh, Z., Harding, A. K., Venter, C., Böttcher, M., & Baring, M. G. 2017, *The Astrophysical Journal*, 839, 80, doi: [10.3847/1538-4357/aa69bf](https://doi.org/10.3847/1538-4357/aa69bf)
- Wadiasingh, Z., Venter, C., Harding, A. K., Böttcher, M., & Kilian, P. 2018, *ApJ*, 869, 120, doi: [10.3847/1538-4357/aaed43](https://doi.org/10.3847/1538-4357/aaed43)
- Ye, Z. P., et al. 2023, *Nature Astron.*, 7, 1497, doi: [10.1038/s41550-023-02087-6](https://doi.org/10.1038/s41550-023-02087-6)

Name	dist (kpc)	d_{DM} (kpc)	$\dot{E}(\times 10^{34} \text{ erg s}^{-1})$	P_b (h)	$M_c(M_\odot)$
PSR J0212+5320	1.1	1.27	-	20.9	0.3
PSR J1023+0038	1.37	0.6	4.3	4.8	0.2
PSR J1036-4353	-	0.4	-	6.2	0.23
PSR J1048+2339	-	1.7	1.2	6.0	0.3
PSR J1227-4853	2.5	1.4	9.0	6.9	0.14
PSR J1302-3258	-	0.96	0.5	15.4	0.15
PSR J1306-40	4.7	1.2	-	26.3	-
PSR J1431-4715	-	1.5	6.8	10.8	0.12
PSR J1526-2744	-	1.3	0.91	4.9	0.083
PSR J1622-0315	-	1.1	0.77	3.9	0.1
PSR J1628-3205	1.2	1.2	1.35	5.0	0.16
PSR J1723-2837	0.75	0.75	4.7	14.8	0.24
PSR J1803-6707	-	1.4	7.4	9.1	0.26
PSR J1816+4510	4.5	2.4	5.2	8.7	0.16
PSR J1908+2105	2.6	2.6	3.2	3.5	0.055
PSR J1910-5320	4.4	1.0	11.5	8.4	0.28
PSR J1957+2516	-	3.1	1.7	5.7	0.1
PSR J2039-5618	1.7	1.7	2.5	5.4	-
PSR J2055+1545	-	3.7	3.83	4.82	0.24
PSR J2129-0429	0.9	0.9	3.9	15.2	0.37
PSR J2215+5135	3.0	3.0	7.4	4.1	0.22
PSR J2339-0533	1.1	0.45	2.3	4.6	0.26
PSR J0407.7-5702	7.0	-	-	-	-
PSR J0427.9-6704	2.4	-	-	8.8	-
PSR J0523-2529	1.1	-	-	16.5	0.8
PSR J0744-2523	1.5	-	-	2.8	-
PSR J0838.8-2829	1.0	-	-	5.1	-
PSR J0935.3+0901	-	-	-	2.44	-
PSR J0940.3-7610	2.0	-	-	6.5	-
PSR J0954.8-3948	1.7	-	-	9.3	-
PSR J1544-1128	3.8	-	-	5.8	-
PSR J1646.5-4406	-	-	-	5.27	-
PSR J1702.7-5655	-	-	-	5.85	-
PSR J2054.2+6904	3.7	-	-	7.5	-
PSR J2333.1-5527	3.1	-	-	6.9	-

Table 2. Table of known Red Backs including candidates (I. F. Nedreaas 2024).

APPENDIX

A. GOLDREICH-JULIAN RATE

The spin-down power of a pulsar is defined as:

$$E(t) = \dot{E}_0 \left(1 + \frac{t}{\tau_{\text{sd}}} \right)^{-2} \quad (\text{A1})$$

The above equation is obtained under the assumption that the energy losses of the pulsar are dominated by magnetic dipole radiation (braking index $n = 3$). In Eq. A1, \dot{E}_0 and τ_{sd} are the initial spin-down energy and the spin-down

Name	dist (kpc)	d_{DM} (kpc)	$\dot{E}(\times 10^{34} \text{ erg s}^{-1})$	P_b (h)	$M_c(M_\odot)$
B1957+20	-	2.5	16	9.2	0.021
PSR J0610-2100	1.5	3.5	0.85	6.9	0.025
PSR J2051-0827	1.04	1.0	0.55	2.4	0.027
PSR J0023+0923	-	0.7	1.6	3.3	0.016
PSR J0251+2606	1.2	0.96	1.8	4.85	0.024
PSR J0636+5128	-	0.5	0.56	1.6	0.007
PSR J0952-0607	-	0.97	-	6.4	0.02
PSR J1124-3653	-	1.7	1.6	5.4	0.027
PSR J1221-0633	-	1.2	2.9	9.27	0.01
PSR J1301+0833	-	0.7	6.7	6.5	0.024
PSR J1311-3430	-	1.4	4.9	1.56	0.008
PSR J1317-0157	-	2.8	0.86	2.14	0.02
PSR J1446-4701	1.4	1.5	3.7	6.7	0.0019
PSR J1513-2550	-	2.0	8.8	4.3	0.02
PSR J1544+4937	-	1.2	1.2	2.8	0.018
PSR J1555-2908	-	7.7	-	5.6	0.05
PSR J1630+3550	-	1.6	2.64	7.58	0.0098
PSR J1641+8049	-	1.7	4.3	2.2	0.04
PSR J1653-0159	0.84	-	0.44	1.25	0.01
PSR J1720-0534	-	0.19	0.85	3.16	0.034
PSR J1731-1847	-	2.5	7.8	7.5	0.04
PSR J1745+1017	-	1.3	0.58	17.5	0.014
PSR J1805+0615	-	3.9	9.3	8.1	0.023
PSR J1810+1744	-	2.0	3.9	3.6	0.044
PSR J1928+1245	-	6.1	0.24	3.3	0.009
PSR J1946-5403	1.23	0.9	-	3.1	0.021
PSR J2017-1614	-	1.1	0.7	2.3	0.03
PSR J2047+1053	-	2.0	1.0	3.0	0.035
PSR J2052+1219	3.9	2.4	3.4	2.75	0.033
PSR J2055+3829	-	4.6	0.36	3.1	0.023
PSR J2115+5448	-	3.4	16.5	3.2	0.02
PSR J2214+3000	-	3.6	1.9	10.0	0.014
PSR J2234+0944	-	1.0	1.7	10.0	0.015
PSR J2241-5236	1.1	0.5	2.5	3.5	0.012
PSR J2256-1024	2.0	0.6	5.2	5.1	0.034
PSR J0336.0+7505	-	-	-	3.7	-
PSR J1406+1222	1.1	-	-	1.03	-
PSR J1408.6-2917	-	-	-	3.4	-
PSR J1838.2+3223	3.1	-	-	4.02	-

Table 3. Table of known Black Widows including candidates (I. F. Nedreaas 2024).

timescale, respectively, and can be expressed as:

$$\begin{aligned}
 \dot{E}_0 &= \frac{8\pi^4 B_0^2 R^6}{3c^3 P_0^4} \\
 \tau_{\text{sd}} &= \frac{3Ic^3 P^2}{4\pi^2 B_0^2 R^6}
 \end{aligned} \tag{A2}$$

where P_0 is the initial spin-down period, B_0 is the magnetic field at the neutron star surface while the inertial momentum is $I = 1.4 \cdot 10^{45} \text{ g cm}^2$ and the pulsar radius $R = 10 \text{ km}$ (J. M. Lattimer & M. Prakash 2007). In order to screen the electric field induced by the rotating magnetic field of the pulsars, particles are extracted from the neutron star surface at the Goldreich-Julian rate :

$$\dot{N}_{\text{GJ}}(t) = \frac{\sqrt{\dot{E}(t)c}}{e} \quad (\text{A3})$$

In this work, we focus on the study of millisecond pulsars and use typical values for this kind of object, namely $B_0 = 10^8 \text{ G}$ and $P_0 = 10^{-3} \text{ s}$, we obtain $\tau_{\text{sd}} \sim \text{Myr}$. We can safely neglect the time dependence and assume that $\dot{E}(t) \sim \dot{E}_0$.

B. INTRABINARY SHOCK RADIUS

One of the possible reasons for the formation of the IBS is the interaction of the two winds. The shock radius then can be calculated according to A. K. Harding & T. K. Gaisser (1990). The solution of the wind pressure balance:

$$R_{\text{sh}} = a \frac{\sqrt{A_{\text{w}}}}{1 + \sqrt{A_{\text{w}}}} \quad (\text{B4})$$

where a is the orbital separation between the pulsar and its companion and

$$A_{\text{w}} = \frac{\dot{E}}{\dot{M}_{\text{w}} v_{\text{w}} c}. \quad (\text{B5})$$

is the ratio of the pulsar wind to the companion wind ram pressure. In the above equation v_{w} represent the escape velocity of the companion and \dot{M}_{w} the mass loss rate of the companion defined in Eq.1 The expression of Eq. B4 is valid under the assumption that $R_{\text{sh}} \ll a - R_{\text{c}}$.